PAPER V

Numerical modeling of radiative heat transfer in water sprays

In: Fire Safety Journal 2006. Vol. 41, No. 1, pp. 76–86.

Available online at www.sciencedirect.com
SCIENCE DIRECT®
Fire Safety Journal 41 (2006) 76–86
FIRE SAFETY JOURNAL
www.elsevier.com/locate/firesaf

Numerical modeling of radiative heat transfer in water sprays

Simo Hostikka[a,*], Kevin McGrattan[b]

[a]VTT Building and Transport, Technical Research Centre of Finland, FI-02044 VTT, Finland
[b]Building and Fire Research Laboratory, National Institute of Standards and Technology, Gaithersburg, MD 20899, USA

Received 28 February 2005; received in revised form 10 August 2005; accepted 1 September 2005
Available online 21 November 2005

Abstract

A numerical method is developed for the transport of polychromatic radiation in polydisperse sprays. The method is implemented within a wide-band radiation solver using the Finite Volume Method. Mie theory is used to compute the absorption and scattering characteristics of the water droplets. The solver is designed to be computationally effective because the simulations of fire scenarios are inherently time-dependent and the radiative transport equation must be solved many times. The model is compared with two sets of experimental data, and a discussion of the results is presented.

Keywords: Water sprays; Radiation model; Scattering calculation; Lagrangian droplets

1. Introduction

Thermal radiation plays a very important role in the development of fires by preheating combustible materials ahead of the flame front. This preheating increases the rate of flame spread, often causing ignition of surfaces without direct flame impingement. Water-based fire suppression systems, like sprinklers and water mist, can reduce the rate of fire spread by blocking thermal radiation. Also, fire fighters use water spray to protect themselves from thermal radiation during assaults on burning buildings.

Water droplets attenuate radiation by absorption and scattering. The relative importance of these mechanisms depends on the droplet size and the wavelength of the radiation. For the fire protection performance of the spray, the geometrical dimensions and water density of the spray are also important. To simulate the radiation transfer in water sprays, one needs to calculate both the transport of energy and the optical properties of the spray. The simplest technique to calculate the transport of energy is to use Lambert–Beer law which assumes that the droplets are totally absorbing or the scattering can be excluded. Ravigururajan and Beltran [1] used Lambert–Beer law for the transport and simple correlations for the optical properties of the droplets to find the optimum droplet size for the attenuation of fire radiation. Since the assumption of pure absorption is not valid in most practical problems, more advanced schemes such as two-flux model [3–6], six-flux model [7] and discrete ordinates method (DOM) or finite volume method (FVM) [8–13] have been developed. Mie theory is typically used for the calculation of the optical properties [2]. It is generally valid for spherical and isolated droplets. An early investigation of the efficiency of large water droplets in the protection from heat radiation was given by Thomas [3]. He derived the expressions for the radiation transmissivity through the droplet cloud using a two-flux model and the geometric optics. Coppalle et al. [4] used a two-flux model and simple approximations of the droplet optical properties allowing for a fast computation of the radiation flux through a layer of water mist. Log [5] used the method of Coppalle et al. to calculate the attenuation of radiation in polydisperse water sprays by assuming that the attenuation effects of the droplet size groups are additive by nature. Yang et al. [6] used Mie theory for the calculation of the absorption and scattering coefficients and scattering phase functions of the water droplets. The spectrally resolved optical properties of water droplets were incorporated into the two-flux model. The model was used to predict the radiation penetration of a monodisperse water mist at different wavelengths.

*Corresponding author. Tel.: +358 20 722 4839; fax: +358 20 722 4815.

0379-7112/$ - see front matter © 2005 Elsevier Ltd. All rights reserved.
doi:10.1016/j.firesaf.2005.09.003

Nomenclature

d	droplet diameter, m
f	normalized droplet number density function
I	total intensity, $\mathrm{Wm^{-2}\,sr^{-1}}$
I_λ	monocromatic intensity, $\mathrm{Wm^{-3}\,sr^{-1}}$
r	droplet radius, m
$\mathbf{s}$	direction vector
$\mathbf{x}$	position vector
U	combined total intensity, $\mathrm{Wm^{-2}}$

Greek symbols

Ω	solid angle, sr
Φ	scattering phase function
χ_f	fraction of forward scattering
ϕ	azimuthal angle
λ	wavelength, m
κ	absorption coefficient, $\mathrm{m^{-1}}$
σ	scattering coefficient, $\mathrm{m^{-1}}$
θ	polar angle

Subscripts

b	blackbody
m	mean
n	band-specific

Keramida et al. [7] used a six-flux model to predict the attenuation in polydisperse water mist. Contributions of different droplet sizes were taken into account by summing the coefficients of a monodisperse spray over the local droplet size distribution. Berour et al. [8] used Mie theory and DOM to investigate the performance of water curtains in fire protection. By stationary simulations of both mono- and polydisperse water sprays in two-dimensional geometry, they studied the effects of droplet size and water curtain thickness on the transmittance and energy balance of the water curtain. Jinbo et al. [9] studied the effect of isotropic scattering approximation on the radiative heat fluxes and temperatures in stationary two-dimensional rectangular media. By comparing the FVM results against benchmark solutions, they concluded that the anisotropic scattering has stronger effect on the relative error of heat flux than the temperature profiles inside the media. Trivic et al. [10] coupled the Mie theory with FVM and studied the radiative transport in monodisperse particle clouds in two dimensions. Similar coupling was made for DOM by Colling et al. [11]. They divided the radiation spectrum to 43–367 bands and solved the RTE for each band in a two-dimensional domain to investigate the performance of water curtains. The use of gray assumption for radiation in monodisperse particle clouds was studied by Consalvi et al. [12]. They also coupled the Mie theory with FVM, and found that the gray model provided correct results for an optical thickness less than 2. The reduction of false scattering was studied in one-dimensional, anisotropically scattering media by Liu et al. [13]. The false scattering appears in the numerical approximation of the in-scattering integral in DOM and FVM methods.

All of the above models have features that limit their applicability on practical fire simulations. Although the one and two-dimensional geometries provide good environment for generation of general rules, like those for water curtains, the practical fire scenarios are always three-dimensional. The same applies for stationary models; the simulations of fire scenarios are inherently time-dependent, and the radiation transport equation must be solved thousands of times for a given scenario. In addition, the coupling of the Mie theory and radiation transport scheme should simultaneously consider the whole spectrum of thermal radiation and distribution of different droplet sizes. The real challenge of the fire model development is to consider these requirements while retaining the computational efficiency. Since radiation typically accounts for about one-third of the energy transport in fires, convection making up the rest, it is logical to require that the computational cost of the radiation solution should not exceed roughly one-third of the overall cost of the calculation.

In this work, a wide-band radiation solver using FVM is implemented within a large eddy simulation fire model. Mie theory is used to compute the radiative properties of the water droplets. The radiative properties of the spray are then computed by averaging the properties of individual droplets over the spectrum and the droplet size distribution. For the fast computation, the spray radiative properties are pre-computed and tabulated as functions of the mean droplet diameter. A simple approximation of the scattering integral is developed to account for the anisotropic scattering.

2. Model description

2.1. Large eddy simulation fire model

The radiation solver and the droplet algorithms described in this paper have been incorporated into fire dynamics simulator (FDS), a computational fluid dynamics (CFD) model of fire-driven fluid flow. The software is developed at the National Institute of Standards and Technology in co-operation with VTT (Finland). The model solves numerically a form of the Navier–Stokes equations appropriate for low-speed, thermally-driven flow with an emphasis on smoke and heat transport from fires. FDS uses a large eddy simulation (LES) model for turbulence. Unlike most Reynolds-averaged Navier stokes

(RANS) solvers, the LES model solves the time scales of the turbulent eddies and therefore requires the small time steps bound by the CFL (Courant, Freidrichs, Lewy) condition. A full description of the model is given in Ref. [14].

2.2. Water droplets

The water spray is modelled as a Eulerian–Lagrangian system, where the gas phase is solved using a Eulerian method and the liquid phase is tracked as numerous Lagrangian particles with mass, momentum and temperature. The Eulerian–Lagrangian approach is currently used in most multidimensional spray simulations because it is simple to implement and computationally efficient [15]. Each droplet, or "parcel", represents a large number of actual droplets. For the statistical representation of the spray, the properties of the parcels are randomly chosen from the given droplet size and velocity distributions. The initial droplet size distribution is expressed in terms of its cumulative volume fraction (CVF), a function that relates the fraction of the water volume (mass) transported by droplets less than a given diameter. The CVF is here represented by a combination of log-normal and Rosin–Rammler distributions [16]

$$F(d)=\begin{cases}\dfrac{1}{\sqrt{2\pi}}\displaystyle\int_0^d \frac{1}{\sigma\, d'}\, \mathrm{e}^{-\frac{[\ln(d'/d_\mathrm{m})]^2}{2\sigma^2}}\, dd' & (d\leqslant d_\mathrm{m}),\\ 1-\mathrm{e}^{-0.693\left(\frac{d}{d_\mathrm{m}}\right)^\gamma} & (d_\mathrm{m}<d),\end{cases} \tag{1}$$

where d_m is the median droplet diameter, and γ and σ are empirical constants equal to about 2.4 and 0.6, respectively. A stratified sampling technique is used for the sampling of the droplets to avoid tracking too many of the numerous tiny droplets and too few of the less numerous larger droplets. In this technique, the range of droplet diameters is divided into a discrete number of intervals. The number of samples from each interval is the same, but the droplets are given weights based on the total volume of the interval. In this work, five intervals are used.

2.3. Wide band model for radiation

The attenuation of radiation is a well-known feature of water (and other) sprays. The attenuation is caused by absorption by the droplets and scattering. The radiation-droplet interaction must therefore be solved for both the accurate prediction of the radiation field and the droplet energy balance. The radiative transport equation (RTE) for spectral intensity I_λ passing through an absorbing/emitting and scattering medium is

$$\mathbf{s}\cdot\nabla I_\lambda(\mathbf{x},\mathbf{s}) = -[\kappa_\lambda(\mathbf{x})+\sigma_\lambda(\mathbf{x})]I_\lambda(\mathbf{x},\mathbf{s})+\kappa_\lambda(\mathbf{x})I_b(\mathbf{x},\lambda) + \frac{\sigma_\lambda(\mathbf{x})}{4\pi}\int_{4\pi}\Phi(\mathbf{s},\mathbf{s}')I_\lambda(\mathbf{x},\mathbf{s}')\,\mathrm{d}\Omega', \tag{2}$$

where I_b is the blackbody source function and $\Phi(\mathbf{s},\mathbf{s}')$ is the scattering phase function giving the scattered intensity from direction $\mathbf{s}'$ to $\mathbf{s}$. Although the emission of water droplets is usually much smaller than the absorption, it is included in the model for consistency and energy conservation. The gas phase absorption and emission are here neglected for simplicity but included in the computations. The computation of the gas phase radiative properties is explained in Ref. [17].

In practical simulations the spectral dependence cannot be solved accurately. Instead, the radiation spectrum is divided into a relatively small number of bands, and a separate RTE is derived for each band by integrating Eq. (2) over the band. The band specific RTEs are

$$\mathbf{s}\cdot\nabla I_n(\mathbf{x},\mathbf{s}) = -[\kappa_n(\mathbf{x})+\sigma_n(\mathbf{x})]I_n(\mathbf{x},\mathbf{s})+\kappa_n(\mathbf{x})I_{\mathrm{b},n}(\mathbf{x}) + \frac{\sigma_n(\mathbf{x})}{4\pi}\int_{4\pi}\Phi(\mathbf{s},\mathbf{s}')I_n(\mathbf{x},\mathbf{s}')\,\mathrm{d}\Omega', \tag{3}$$

where κ_n is the mean absorption coefficient inside the band. The source term can be written as a fraction of the blackbody radiation

$$I_{\mathrm{b},n}=F_n(\lambda_\mathrm{min},\lambda_\mathrm{max})\sigma T_i^4/\pi, \tag{4}$$

where σ is the Stefan–Boltzmann constant and λ_min and λ_max are the limits of the n'th band. The calculation of factors F_n is explained in Ref. [2]. When the integrated intensities corresponding to the bands are known, the total intensity and combined total intensity are calculated by summing over all the bands

$$I(\mathbf{x},\mathbf{s})=\sum_{n=1}^{N_\mathrm{b}} I_n(\mathbf{x},\mathbf{s}), \tag{5}$$

$$U(\mathbf{x})=\sum_{n=1}^{N_\mathrm{b}} U_n(\mathbf{x})=\sum_{n=1}^{N_\mathrm{b}}\int_{4\pi} I_n(\mathbf{x},\mathbf{s})\,\mathrm{d}\Omega. \tag{6}$$

To include the most important absorption bands of water and CO_2, the most important gaseous species in fire simulations, six radiation bands are used. The limits of the bands are shown in Table 1. Even with a reasonably small number of bands, the solution of N_b RTEs is very time consuming. Fortunately, in most large-scale fire scenarios soot is the most important combustion product controlling the thermal radiation from the fire and hot smoke. As the radiation spectrum of soot is continuous, a gray gas behaviour can be assumed ($N_\mathrm{b}=1$).

2.4. Averaging over the droplet size distribution

The local absorption and scattering coefficients are functions of the local droplet size distribution:

$$\kappa_\lambda(\mathbf{x})=\int_0^\infty N(r,\mathbf{x})\,C_\mathrm{a}(r,\lambda)\,\mathrm{d}r,$$
$$\sigma_\lambda(\mathbf{x})=\int_0^\infty N(r,\mathbf{x})\,C_\mathrm{s}(r,\lambda)\,\mathrm{d}r, \tag{7}$$

where $N(r,\mathbf{x})$ is the number of droplets having radius between r and $r+\delta r$ at position $\mathbf{x}$. The absorption and scattering cross sections, C_a and C_s, are calculated using Mie theory. In practical simulations, it is impossible to perform these integrations at each position at every time

Table 1
Limits of the spectral bands for a 6-band model.

Band	1	2	3	4	5	6
Major Species	Soot	CO_2 H_2O, Soot	Soot	CO_2 Soot	H_2O, Soot	Soot
ν (1/cm)	10000	3800	3400	2400	2174	1000	50
λ (μm)	1.00	2.63	2.94	4.17	4.70	10.0	200

step. Instead, we assume that the local droplet number density function has the same functional form regardless of position, with only the mean diameter varying from point to point. The local size distribution can now be expressed by

$$N(r,\mathbf{x}) = N'(\mathbf{x}) f(r, d_m(\mathbf{x})) \tag{8}$$

and the local absorption and scattering coefficients can be determined by averaging over the initial droplet size distribution function

$$\kappa_\lambda(\mathbf{x}) = N'(\mathbf{x}) \int_0^\infty f(r, d_m(\mathbf{x}))\, C_a(r,\lambda)\, dr,$$
$$\sigma_\lambda(\mathbf{x}) = N'(\mathbf{x}) \int_0^\infty f(r, d_m(\mathbf{x}))\, C_s(r,\lambda)\, dr. \tag{9}$$

For the numerical implementation, it is useful to write the above equation in the form

$$\kappa_\lambda(\mathbf{x}) = A_d(\mathbf{x}) \int_0^\infty \frac{f(r, d_m(\mathbf{x}))\, C_a(r,\lambda)}{\pi (d_m(\mathbf{x})/2)^2}\, dr,$$
$$\sigma_\lambda(\mathbf{x}) = A_d(\mathbf{x}) \int_0^\infty \frac{f(r, d_m(\mathbf{x}))\, C_s(r,\lambda)}{\pi (d_m(\mathbf{x})/2)^2}\, dr, \tag{10}$$

where A_d is the total cross sectional area of the droplets per unit volume. We approximate $A_d(\mathbf{x}) \approx \rho_d(\mathbf{x}) / [2\rho_w d_m(\mathbf{x})/3]$, where ρ_w is the density of water and $\rho_d(\mathbf{x})$ is the water mass per unit volume, which is provided by the droplet tracking algorithm. The integrals of Eq. (10) can be calculated in advance and stored in tables for different values of d_m.

The absorption and scattering cross sections and the scattering phase function are calculated using the "MieV" algorithm developed by Wiscombe [18]. The optical properties of water are taken from Ref. [19]. Mie theory is generally valid for homogenous isotropic spherical objects embedded in a homogenous, isotropic, dielectric and infinite medium. As the current work considers relatively low speed droplets in air, most of the above assumptions are valid. The interference between the droplets can be neglected when the center to center spacing is more than about 3 diameters. In terms of mean diameter and average spacing the interference condition is

$$d_m(\mathbf{x}) \sqrt[3]{N'(\mathbf{x})} < \frac{1}{3}. \tag{11}$$

2.5. Approximation of the scattering integral

An accurate computation of the in-scattering integral on the right-hand side of Eq. (2) would be extremely time consuming. It is here approximated by dividing the total 4π solid angle into a "forward angle" $\delta\Omega^l$ and the corresponding "ambient angle" $\delta\Omega^* = 4\pi - \delta\Omega^l$. For compatibility with the FVM solver, the forward angle is set equal to the control angle resulting from the angular discretization. However, the forward angle is assumed to be symmetric about the center of the corresponding control angle. Within the forward angle $\delta\Omega^l$, the intensity is $I_\lambda(\mathbf{x},\mathbf{s})$. Within the ambient angle, it is approximated as

$$U^*_\lambda(\mathbf{x}) = \frac{U_\lambda(\mathbf{x}) - \delta\Omega^l I_\lambda(\mathbf{x},\mathbf{s})}{\delta\Omega^*} \tag{12}$$

where $U_\lambda(\mathbf{x})$ is the combined spectral intensity at wavelength λ. The in-scattering integral can now be approximated as

$$\frac{\sigma_\lambda(\mathbf{x})}{4\pi} \int_{4\pi} \Phi(\mathbf{s},\mathbf{s}') I_\lambda(\mathbf{x},\mathbf{s}')\, d\Omega' = \sigma_\lambda(\mathbf{x})[\chi_f I_\lambda(\mathbf{x},\mathbf{s}) + (1-\chi_f) U^*_\lambda(\mathbf{x})], \tag{13}$$

where $\chi_f = \chi_f(r,\lambda)$ is a fraction of incoming intensity originally within solid angle $\delta\Omega^l$ that is scattered into the same angle $\delta\Omega^l$. An effective scattering coefficient is now defined as

$$\bar\sigma_\lambda(\mathbf{x}) = \frac{4\pi A_d(\mathbf{x})}{4\pi - \delta\Omega^l} \int_0^\infty f(r, d_m(\mathbf{x}))\left[1 - \chi_f(r,\lambda)\right] \frac{C_s(r,\lambda)}{\pi d_m(\mathbf{x})^2/4}\, dr. \tag{14}$$

By using the above definition of $\bar\sigma_\lambda(\mathbf{x})$ and integrating the RTE over the spectrum we get a band-specific RTE

$$\mathbf{s}\cdot\nabla I_n(\mathbf{x},\mathbf{s}) = -[\kappa_n(\mathbf{x}) + \bar\sigma_n(\mathbf{x})] I_n(\mathbf{x},\mathbf{s}) + \kappa_n(\mathbf{x}) I_{b,n}(\mathbf{x}) + \frac{\bar\sigma_n(\mathbf{x})}{4\pi} U_n(\mathbf{x}), \tag{15}$$

where the source function is based on the average droplet temperature within a cell.

During the simulation, the local values of κ_n and $\bar\sigma_n$ are interpolated from one-dimensional tables using $d_m(\mathbf{x})$. A Planck spectrum, used in the wavelength averaging, is calculated using some appropriate value for temperature. This "radiation temperature" T_{rad} should be selected to represent the temperature of a radiating flame.

A formula for χ_f was previously derived by Yang et al. [6].

$$\chi_f(r,\lambda) = \frac{1}{\delta\Omega^l} \int_0^{\mu_x} \int_0^{\mu_x} \int_{\mu_{d,0}}^{\mu_{d,\pi}} \times \frac{P_0(\theta_d)}{\left[(1-\mu^2)(1-\mu'^2) - (\mu_d - \mu\mu')^2\right]}\, d\mu_d d\mu d\mu', \tag{16}$$

where μ_d is a cosine of the scattering angle θ_d and $P_0(\theta_d)$ is a single droplet scattering phase function

$$P_0(\theta_d) = \frac{\lambda^2\left(|S_1(\theta_d)|^2 + |S_2(\theta_d)|^2\right)}{2C_s(r,\lambda)} \tag{17}$$

and $S_1(\theta_d)$ and $S_2(\theta_d)$ are the scattering amplitudes, given by Mie theory. When χ_f is integrated over the droplet size distribution in Eq. (14), it is multiplied by $C_s(r,\lambda)$. It is therefore $|S_1|^2 + |S_2|^2$, not $P_0(\theta_d)$, that is integrated. Some examples of phase function $P_0(\theta_d)$ are shown in Fig. 1, at different values of droplet size parameter $X \equiv 2\pi r/\lambda$. At small values of X the phase function is almost constant over the scattering angle, and at high values the (large droplets, small wavelength) the energy is scattered close to the forward direction.

The integration limit μ_x is the cosine of the polar angle defining the boundary of the symmetric control angle $\delta\Omega^l$

$$\mu_x = \cos(\theta^l) = 1 - \frac{2}{N_\Omega}, \tag{18}$$

where N_Ω is the total number of control angles. The limits of the innermost integral are

$$\mu_{d,0} = \mu\mu' + \sqrt{1-\mu^2}\sqrt{1-\mu'^2},$$
$$\mu_{d,\pi} = \mu\mu' - \sqrt{1-\mu^2}\sqrt{1-\mu'^2}. \tag{19}$$

One weakness of the modeling approach is that a higher N_Ω does not always imply better accuracy, because less and less radiation is scattered into the forward control angle. That is, the direction information of the scattered energy at angles $\theta > \theta^l$ is lost, and the energy is divided evenly over the ambient angle $\delta\Omega^*$.

2.6. Numerical solution of RTE

The radiative transport (3) is solved using the finite volume method (FVM) for radiation [20]. The intensities on the cell boundaries are calculated using a first order upwind scheme. The solution method of the discretized RTE is based on an explicit marching sequence [21], where the physical space is swept in the propagation direction of the intensity and the intensities can be solved explicitly from an algebraic equation. Iterations are needed only to account for the reflective boundaries and scattering. However, this is seldom necessary in practice, because of the small time step needed by the fluid flow solver.

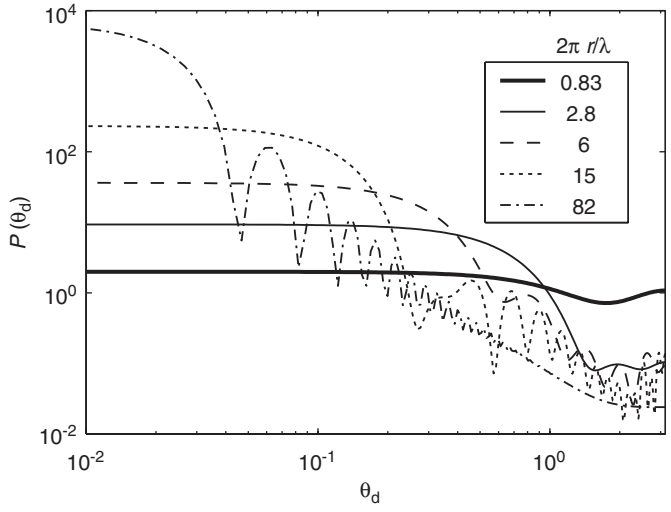

Fig. 1. Normalized unpolarized phase function of a single droplet.

The spatial discretization for the RTE solver is the same as for the fluid solver. The distribution of the angles is based on empirical rules that attempt to produce equal control angles $\delta\Omega^l = 4\pi/N_\Omega$, where N_Ω is the number given by the user. The polar angle, θ, is first divided into N_θ bands, where N_θ is an even integer. Each θ-band is then divided into $N_\phi(\theta)$ parts in the azimuthal (ϕ) direction. $N_\phi(\theta)$ must be divisible by 4. The number of θ-bands is

$$N_\theta = 1.17\ N_\Omega^{1/2.26} \tag{20}$$

rounded to the nearest even integer. The number of ϕ-angles on each band is

$$N_\phi(\theta) = \max\{4, 0.5\,N_\Omega\,[\cos(\theta^-) - \cos(\theta^+)]\} \tag{21}$$

rounded to the nearest integer divisible by 4. θ^- and θ^+ are the lower and upper bounds of the θ-band, respectively. Finally, the exact N_Ω is calculated as

$$N_\Omega = \sum_{i=1}^{N_\theta} N_\phi(\theta_i). \tag{22}$$

The angular discretization is symmetric with respect to the planes $x = 0$, $y = 0$, and $z = 0$. This symmetry has three important benefits: first, it avoids the problems caused by the fact that a first order upwind scheme is more diffusive in non-axial directions. Second, the treatment of symmetric boundaries becomes very simple. Third, it avoids so-called "overhang" situations, where the sign of the intensity direction vector components is changed inside the control angle. These "overhangs" can make the system of linear equations more complicated.

Computational cost is always an issue in time-dependent simulations, especially in simulations that are bound by the CFL condition. To reduce the cost of the radiation solution, the radiation solver is typically not called at every time step of the hydrodynamic solver. For time steps where the radiation is not being updated, only the radiative loss term must be updated to maintain the time accuracy of the energy equation. More savings can be achieved by updating only a fraction of the control angles for a given call to the radiation solver. The effect of this kind of cost reduction is demonstrated in Fig. 2. The upper figure shows the time development of the combined total intensity U inside a hydrocarbon pool flame in some arbitrary units. Fig. 2(b) shows similar results inside a water spray with external radiation source. Local gas temperature and droplet diameter are shown for reference. As can be seen, the cost reduction has a slight time-averaging effect. These cost–saving measures should not be applied when the exact

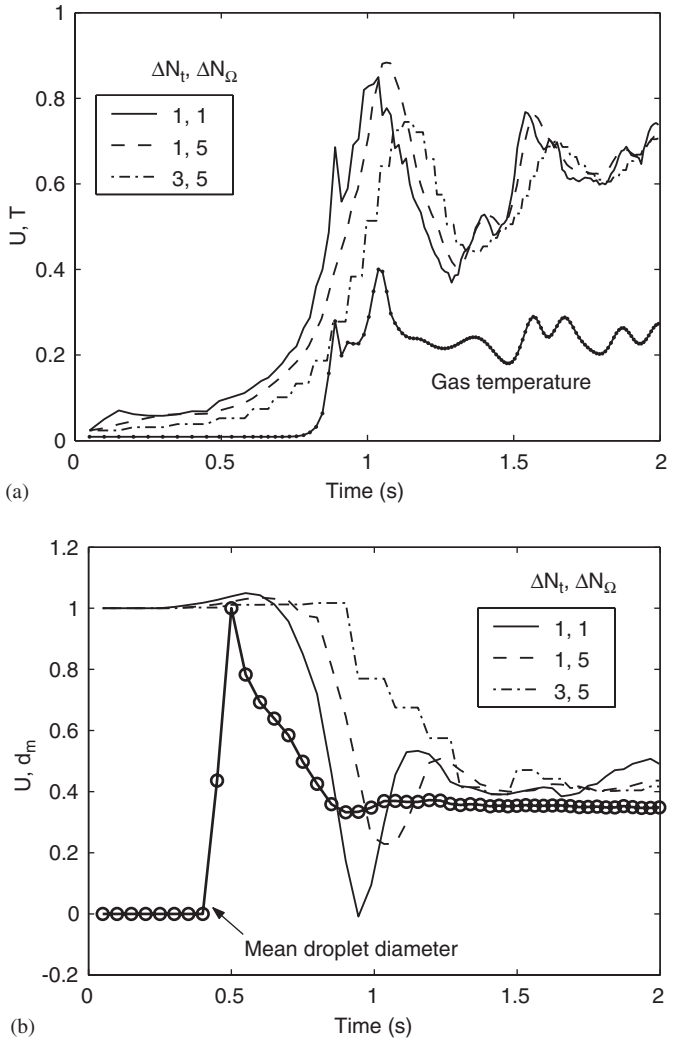

Fig. 2. The effect of the temporal and angular increments on the combined intensity in (a) pool flame and (b) water spray. The units are arbitrary. The radiation solver is called every ΔN_t time steps of the hydrodynamic solver and every ΔN_Ω control angles are updated per call.

time dependence of the turbulence-radiation interaction is needed. Numerical experiments have shown that for practical fire simulations, calling the radiation every 3 time steps and updating 1 out of 5 control angles per call gives acceptable results.

3. Results and discussion

3.1. Large-scale experiment

The first validation test is the simulation of experiment conducted by Murrel et al. [22]. They measured the attenuation of thermal radiation passing through a water spray using a heat flux gauge. The schematics of the system are shown in Fig. 3. The radiation was produced by a heat panel, one meter square, at 900 °C. The horizontal distance from the radiation panel to the spray nozzle was 2 m and to the measurement point 4 m. The nozzles were positioned at a height 0.24 m above the panel upper edge. The heat flux gauge was positioned at the line passing through the center of the panel. The attenuation of radiation was defined as $(q_0 - q_s)/q_0$, where q_0 is the initial radiative heat flux, measured without a spray, and q_s is the heat flux measured during the spray operation. The purpose of the simulation is to compare the measured and simulated attenuation of radiation at different flow conditions.

The computational domain was 4 m wide, 2 m deep and 3 m high. The vertical and top boundaries were open, and the bottom of the domain was a solid floor. The nozzle was positioned horizontally in the center of the domain at height 2.24 m. Three different nozzles were simulated. Each nozzle was a full-cone type industrial nozzle. The simulations were performed at eight different flow rates.

In the experiments, Murrel et al. [22] did not measure the mean droplet diameters in the vicinity of the nozzles, but 0.7 m below the nozzle, i.e. at the height of the heat flux measurement point. The droplet size boundary condition d_m (BC) was therefore determined by iterating d_m (BC) until the simulated and measured mean diameters at the measurement location were equal, with a few percent tolerance. The iteration was performed for all nozzle-flow rate combinations. The initial droplet size distribution was assumed to have the functional form of Eq. (1). The measured and corresponding BC mean diameters are listed in Table 2. For nozzle D, the measured mean droplet diameter increased with increasing pipe pressure Δp between 1 and 3 bar, and then dropped sharply between 5 and 6 bar. The experimental results defy a commonly used scaling relation for water droplets, which states that $d_m \propto \Delta p^{-1/3}$ [23,24]. The measured mean diameters (shown in parentheses) were therefore replaced by values that follow the trend found for nozzles A and B. For the parameters γ and σ controlling the width of the droplet size distribution, the default values 2.43 and 0.6 were used. Numerical experiments showed that attenuation results are relatively insensitive to the small variations of γ and σ. The droplet velocities on the inflow boundaries were set equal to the measured vertical velocity component 0.7 m below the nozzle. At the chosen flow rates, the interference

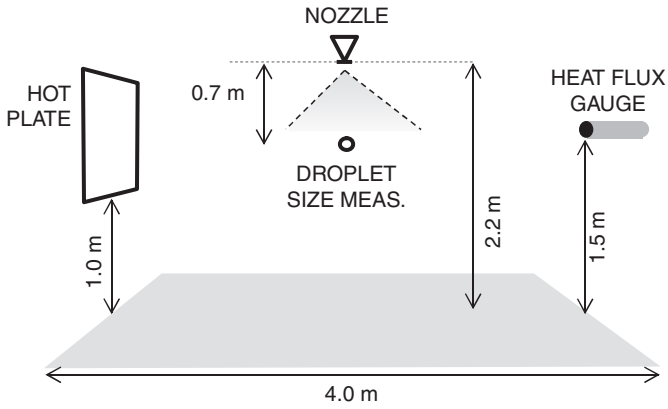

Fig. 3. Schematics of the experiment of Murrel et al. [22].

Table 2
Boundary conditions of the A, B and D nozzles

	Nozzle A			Nozzle B			Nozzle D		
Δp (bar)	Flow (L/min)	d_m (exp.) (μm)	d_m (BC) (μm)	Flow (L/min)	d_m (exp.) (μm)	d_m (BC) (μm)	Flow (L/min)	d_m (exp.) (μm)	d_m (BC) (μm)
1	0.350	268	353	1.40	392	552	2.60	691	768
2	0.550	175	190	1.83	266	398	3.75	327 (753)	420
3	0.625	110	110	2.00	167	212	4.50	276 (794)	377
4	0.700	104	104	2.25	162	209	5.00	235 (638)	295
5	0.750	102	102	2.50	115	120	5.75	200 (550)	236
6	0.875	102	102	2.75	126	140	6.00	182	225
7	0.950	93	93	3.00	156	212	6.75	178	219
8	1.00	126	126	3.25	148	186	7.50	160	185

Four of the nozzle D measurements (shown in parentheses) were assumed erroneous and replaced by values having the same trend as nozzles A and B.

condition (Eq. (11)) was satisfied in all parts of the computational domain.

The sensitivity to the numerical and other parameters was first studied. For angular discretization $N_\Omega = 1000$ was found to be high enough, as can be seen in Fig. 4(a). The figure shows the change of combined total intensity U from its initial value U_0 on the line passing through the spray from the heat panel ($x = -2$ m) to the heat flux measurement point ($x = 2$ m). The spray nozzle D and pressure of 4 bar were used for the tests. On the left-hand side of the spray U first increases due to the scattering from the spray. Strong attenuation is then seen at a distance of 0.4 m inside the spray. The results are independent of the size of the grid cells, as shown in Fig. 4(b), where the attenuation at the different flow rates of nozzle D is plotted for 10 and 5 cm grid cells. The same figure also shows that the use of multiple radiation bands and gas phase absorption do not change the attenuation results considerably. For the calculation of the final results, the following numerical parameters were used: 10 cm grid cells, 1000 control angles, only one spectral band (gray assumption) and no gas phase absorption. For each case, 15 s of real time was simulated and the attenuation results were time averaged over the last 10 s. The simulation of 15 s required about 160 s on a single 3.0 GHz processor of a personal computer. Without the cost-saving measures of the radiation solver, i.e. if all the radiation directions were solved at every time step, the required CPU time was about 1380 s.

The measured and predicted attenuation results for all three nozzles and flow rates are compared in Fig. 5. Since a good general agreement was found for all three nozzles, and the results of the individual nozzles are well distinct in the flow-rate vs. attenuation space, we can assume that the model can properly take into account both the effect of the water load and the effect of the droplet size distribution. Only the mid-range flow rates of nozzle B and the highest flow rates of nozzle D show sizable discrepancies. These discrepancies are probably caused by a combination of measurement errors and model inaccuracy. The droplet size measurements, in particular, are difficult to conduct in large scale sprays. Some uncertainty is also related to the simulation boundary conditions of the droplet size.

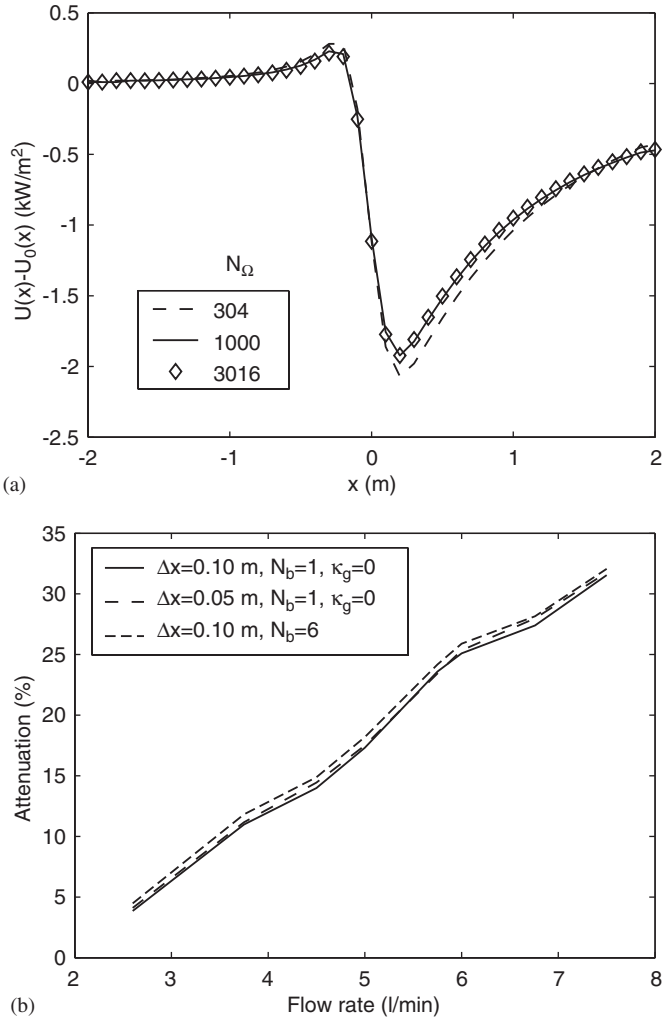

Fig. 4. (a) The effect of the angular discretization on change of combined intensity. (b) The effect of grid cell size, N_Ω and gas phase absorption on the attenuation at the measurement point.

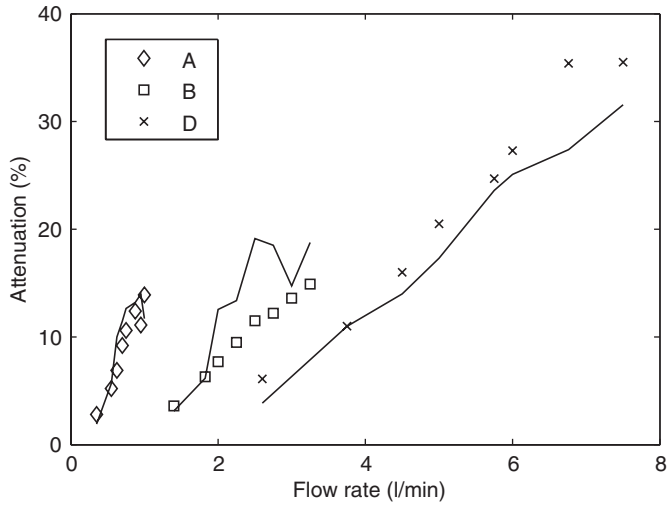

Fig. 5. Comparison of measured and predicted attenuation of thermal radiation at spray nozzles A, B and D, and different flow rates. Lines represent simulation results.

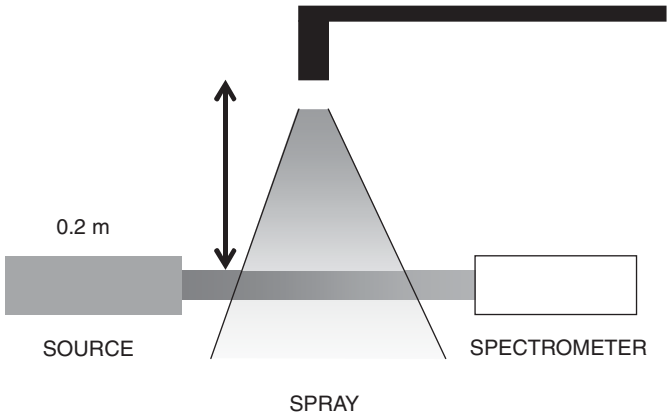

Fig. 6. Schematics of the experiment of Dembele et al. [25].

3.2. Small-scale experiment

In the second validation exercise, the experiments of Dembele et al. [25] were simulated. They measured the attenuation of a collimated radiation beam passing through a water spray using a Fourier infrared spectrometer. The radiation source was a tungsten filament inside a silica tube. Its emission spectrum was close to that of a blackbody at 1300 °C. The spray was produced with 1, 2 or 3 hydraulic nozzles arranged in a row, and the measurements were made 20 cm below the nozzles at different flow rates. The schematics of the scenario are shown in Fig. 6. Again, only total intensity data are compared and the spectral information available in the experiment is not used.

The simulations were performed at four different flow rates. The computational domain was a 40 cm cube with open, constant-pressure boundaries. The nozzles were placed 5 cm below the top of the computational domain, and the radiation source was located 20 cm below the nozzles. A numerical grid of $20 \times 20 \times 20$ cells was used for the flow solver and 1000 angles for FVM. Six radiation bands were used, but the gas phase absorption was neglected. At each flow rate, at least 15 s of constant flow was simulated to get a converged time-averaged value for the attenuation. The uncertainty of the time-averaging process is less than 10% for the attenuation results. A simulation of 15 s with 6 bands took about 320 s on a single 3.0 GHz CPU. With only one band, the computation time would drop down to 90 s.

Modeling a collimated radiation beam is difficult with the current implementation of FVM due to the symmetric discretization of the unit sphere into solid angles. To alleviate the problem, the radiation source in this exercise was modeled simply as a 4 cm by 4 cm rectangular surface, radiating in all directions. Because the air surrounding the water spray was cool, practically transparent to radiation, and did not contain any scattering particles, it did not contribute to the predicted intensity field behind the spray. Therefore, the comparison with the measurements is valid on the opposite side of the spray, but not in the other directions.

Dembele et al. measured the droplet size distribution 20 cm below the nozzle for each flow rate. The droplet size boundary conditions were determined using a procedure similar to the large scale scenario. Again, the droplet size distribution function Eq. (1) was assumed, with default values for the width parameters γ and σ. The measured and corresponding mean diameter boundary conditions are given in Table 3. For this exercise, the velocity of the droplets at the inflow boundary was found from a simple geometrically-based relationship between the flow velocity and distance. The cone angle of the nozzle was measured from the illustrations of Ref. [25], and set to 130°.

An example of the time-averaged spray pattern at a flow rate of 0.22 L/min is shown in Fig. 7. The contours of the droplet mean diameter d_m are shown in the vertical plane cutting through the nozzle. The initial conical shape of the spray is very soon squeezed to a vertical column by the entraining air. The core of the spray contains smaller droplets than the edge because the larger droplets have higher momentum and are not as easily entrained as the smaller droplets. This suggests that the droplet size measurement just below the nozzle does not necessarily represent the size distribution of the whole spray.

In the radiation model, we approximate the local droplet size distributions by the initial functional form. The validity of this approximation is demonstrated in Fig. 8. The droplet diameters were sampled from two locations of a simulated water spray. The number densities of the sampled distributions are shown as vertical bars. The mass-weighted mean diameters were calculated from the sampled distributions, and corresponding theoretical density functions (Eq. (1)) were drawn on the figure. As can be seen, the approximation holds well within the core of the spray, but fails near the edge of the spray. Fortunately, the core area

Table 3
Boundary conditions of the TG03 spray droplets

Flow rate (L/min/nozzle)	d_m (exp.) (μm)	d_m (BC) (μm)	Velocity (BC) (m/s)
0.14	187	264	0.33
0.22	135	187	0.51
0.28	115	155	0.65
0.33	104	140	0.75

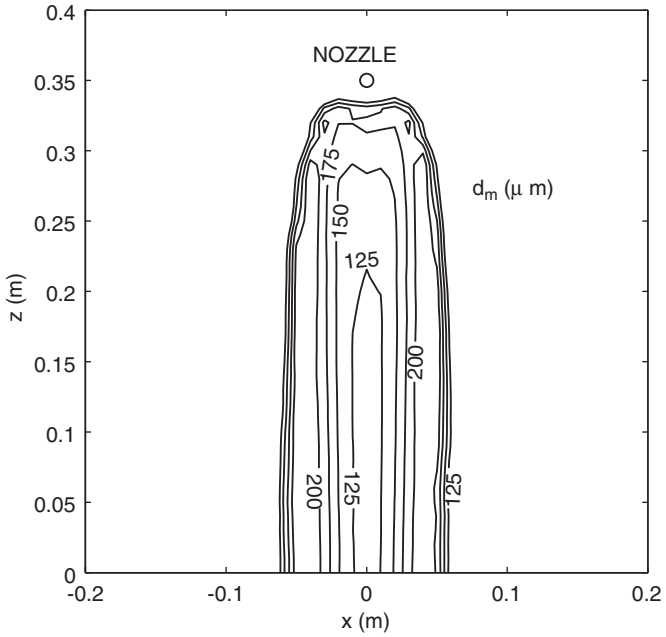

Fig. 7. Contours of the time averaged droplet mean diameter field at 0.22 L/min flow rate. The co-ordinates correspond to the computational domain used.

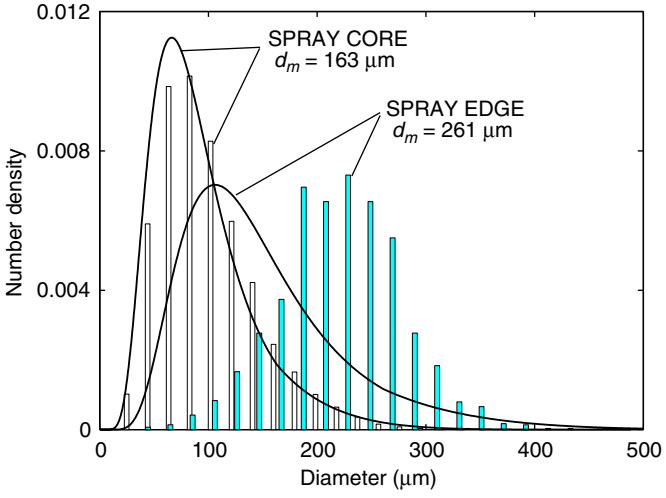

Fig. 8. Theoretical and sampled size distributions in the core and close to the edge of the spray. Lines are the assumed probability density functions and bars are the sample histograms from the simulation.

is much more important for the radiation attenuation because the number density is higher there than at the edge. The approximation may also fail if the spray penetrates a hot environment, because the evaporation rate depends on the droplet radius, and probably affects the shape of the size distribution.

In this scenario, the independence of the spatial and angular resolutions is very difficult to achieve. The effect of the spatial resolution was studied by reducing the cell size from 2.0 cm to 1.0 cm. As a result, the attenuation in the case of one nozzle at 0.14 L/min flow rate changed from 8.3% to 11.4%, with 10.0% being the experimental value. Unfortunately, the 1 cm grid cells could not be used for the all cases due to the strong increase of computational cost. The effect of angular resolution is studied in Fig. 9 by plotting the combined total intensity $U(\mathbf{x})$ at the horizontal line passing through the center of the radiation source at different values of N_Ω. Fig. 9(a) shows that $U(\mathbf{x}) \approx 450\,\mathrm{kW/m^2}$ close to the source and $U(\mathbf{x}) \approx 10\,\mathrm{kW/m^2}$ in the spray region. For $N_\Omega \geqslant 1000$, the absolute value seems well converged but the change of the field from the initial state in Fig. 9(b) shows no convergence even at $N_\Omega = 3000$.

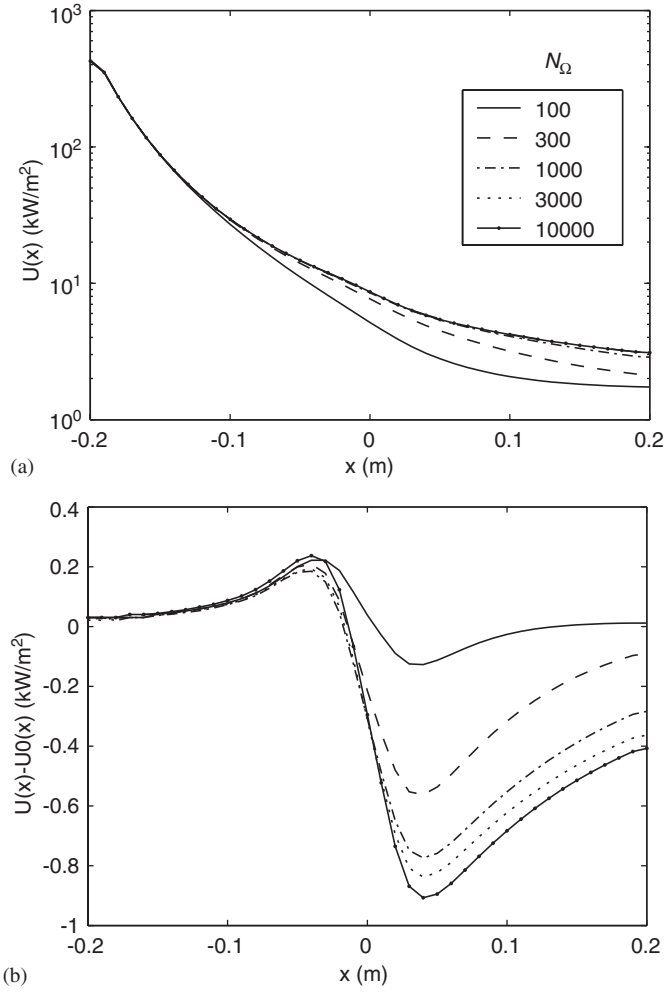

Fig. 9. The effect of the angular accuracy on (a) combined total intensity U and (b) the change of U.

Table 4
Results of the TG03 spray simulation

Flow rate (L/min/nozzle)	Attenuation (%) 1 nozzle		2 nozzles		3 nozzles	
	Measured	Predicted	Measured	Predicted	Measured	Predicted
0.14	10.0	8.3	12.3	16.5	17.3	23.5
0.22	18.6	18.0	25.2	32.4	34.0	43.0
0.28	26.4	26.3	35.9	43.3	46.8	58.1
0.33	33.8	32.1	44.9	51.0	57.3	65.4

There are two reasons why the results are sensitive to the angular resolution. First, the radiation source is very small compared to the overall size of the domain. When 2 cm grid cells are used, the radiation source is spanned by only four cells. The second reason is that the radiation is monitored at the line perpendicular to the source plane. Despite the smoothing effect of the numerical diffusion typical of a first-order solution scheme, the ray effect is practically unavoidable for this direction because the solid angles used in the FVM solver do not overlap with the domain axis. As a result, a large number of solid angles may be needed to reach converged results at the axis perpendicular to the small source. Neither of the above reasons is directly related to the scattering solver, but to the applied angular discretization and FVM schemes. However, at this point one should remember that the numerical method to calculate the forward scattering fraction χ_f is not fully consistent with the angular discretization, i.e. the accuracy is not consistently improved when the number of control angles is increased. Therefore, the final results are given for $N_\Omega = 1000$. In addition to the above, the spectral resolution (use of multiband model) was also found to be important, especially in the case of low flow rate (optically thin case). Since the difficulties associated with the grid and angular dependence are much related to the small radiation source, rarely found in fire simulations, the results should provide valuable information on the capability of the model to capture the underlying physical processes.

Finally, the measured and simulated attenuation results are compared in Table 4. In the case of only one nozzle, the agreement is very good, taking into account the unavoided dependence on the grid and angular resolutions. The root-mean-square error between the predicted and measured attenuations is only 1.3%-units. When more nozzles are put between the source and the measurement point, the attenuation is clearly over-predicted. The root-mean-square errors for two and three nozzles are 6.4 and 8.8%-units, respectively. One possible reason for the over-prediction is the droplet coalescence, which is not taken into account by the model. Coalescence happens as a result of the hydrodynamic interaction between adjacent sprays [25]. This explanation is supported by the finding that while the predicted attenuations with two and three nozzles increase roughly by factors two and three from the values corresponding to the one nozzle, the experimental results increase only by factors 1.3 and 1.8.

4. Conclusions

A numerical model of radiation transport in polydisperse water spray has been described. The turbulent fluid flow is modeled using a low Mach number large eddy simulation and liquid droplets are tracked using a Lagrangian approach. A finite volume method for radiation transport is extended for the droplet absorption and scattering.

In transient engineering applications, the computational efficiency is of equal importance to the accuracy of the physical models. Because of the limitations in computational speed, only a small sample of the droplet population can be explicitly tracked, leading to inaccuracies in the droplet size statistics needed for the absorption and scattering routines. Stratified sampling techniques can be used to improve the accuracy of the sampled distributions. In the radiation solver, the approximation of the incoming intensity by combined intensity U and the efficient use of look-up tables allow the reasonably accurate solution of the droplet scattering with only a small additional cost.

The simulations of two validation scenarios showed that the current model can predict the attenuation of thermal radiation in water sprays when the hydrodynamic interaction between the droplets is weak. Modeling of interacting sprays would require an implementation of the droplet coalescence model, increasing the cost of the entire flow calculation.

Acknowledgements

The authors wish to acknowledge Dr. Jukka Vaari from VTT, and Dr. Howard Baum and Dr. John Widmann from NIST for the fruitful discussions and advice.

References

[1] Ravigururajan TS, Beltran MR. A model for attenuation of fire radiation through water droplets. Fire Safety J 1989;15:171–81.
[2] Siegel R, Howell JR. Thermal radiation heat transfer, third ed. Philadelphia: Hemisphere Publishing Corp; 1992.
[3] Thomas PH. Absorption and scattering of radiation by water sprays of large drops. Brit J Appl Phys 1952;3:385–93.

[4] Coppalle A, Nedelka D, Bauer B. Fire protection: water curtains. Fire Safety J 1993;20:241–55.
[5] Log T. Radiant heat attenuation in fine water sprays. In: Interflam 96, Seventh international fire science and engineering conference, Interscience Communications; 1996, p. 425–34.
[6] Yang W, Parker T, Ladouceur HD, Kee RJ. The interaction of thermal radiation and water mist in fire suppression. Fire Safety J 2004;39:41–66.
[7] Keramida EP, Karayannis AN, Boudouvis AG, Markatos NC. Numerical modeling of radiant heat attenuation through water mist. Combust Sci Technol 2000;159:351–71.
[8] Berour N, Lacroix D, Boulet P, Jeandel G. Radiative and conductive heat transfer in a nongrey semitransparent medium. Application to fire protection curtains. J Quant Spectrosc Radiat Transfer 2004;86: 9–30.
[9] Jinbo H, Liming R, Heping T. Effect of anisontropic scattering on radiative heat transfer in two-dimensional rectangular media. J Quantit Spectrosc Radiat Transfer 2003;78:151–61.
[10] Trivic DN, O'Brien TJ, Amon CH. Modeling the radiation of anisotropically scattering media by coupling Mie theory with finite volume method. Int J Heat Mass Transfer 2004;47:5765–80.
[11] Collin A, Boulet P, Lacroix D, Jeandel G. On radiative transfer in water spray curtains using the discrete ordinates method. J Quantit Spectrosc Radiat Transfer 2005;92:85–110.
[12] Consalvi JL, Porterie B, Loraud JC. On the use of gray assumption for modeling thermal radiation through water sprays. Numer Heat Transfer, Part A 2003;44:505–19.
[13] Liu LH, Ruan LM, Tan HP. On the discrete ordinates method for radiative heat transfer in anisotropically scattering media. Int J Heat Mass Transfer 2002;45:3259–62.
[14] McGrattan KB, Baum HR, Rehm RG, Forney GP, Floyd JE, Prasad K, Hostikka S. Fire dynamics simulator (Version 3), Technical Reference Guide, Technical Report NISTIR 6783, 2002 edition. National Institute of Standards and Technology, Gaithersburg, Maryland, November 2002.
[15] Are S, Hou S, Schmidt DP. Second-order spatial accuracy in Lagrangian–Eulerian Spray Calculations. Numer Heat Transfer, Part B 2005;48:25–44.
[16] Chan TS. Measurements of water density and droplet size distributions of selected ESFR sprinklers. J Fire Prot Eng 1994;6(2):79–87.
[17] Hostikka S, McGrattan KB, Hamins A. Numerical modeling of pool fires using LES and finite volume method for radiation, In: Fire safety science—proceedings of the seventh international symposium. International Association for Fire Safety Science; 2003, p. 383–94.
[18] Wiscombe W. Mie scattering calculations: advances in technique and fast, vector-speed computer codes, NCAR Technical Note NCAR/TN-140+STR, National Center For Atmospheric Research, 1979 (revised 1996).
[19] Hale GM, Querry MR. Optical constants of water in the 200 nm to 200 μm wavelength region. Appl Opt 1973;12:555–63.
[20] Raithby GD, Chui EH. A finite-volume method for predicting radiant heat transfer in enclosures with participating media. J Heat Transfer 1990;112(2):415–23.
[21] Kim SH, Huh KY. Assessment of the finite-volume method and the discrete ordinate method for radiative heat transfer in a three-dimensional rectangular enclosure. Numer Heat Transfer, Part B 1999;35:85–112.
[22] Murrel JV, Crowhurst D, Rock P. Experimental study of the thermal radiation attenuation of sprays from selected hydraulic nozzles. In: Proceedings of Halon options technical working conference. The University of New Mexico: Albuquerque; 1995. p. 369–78.
[23] You H. Investigation of spray patterns of selected sprinklers with the FMRC drop size measuring system. In: Fire safety science—proceedings of the first international symposium. International Association for Fire Safety Science; 1986. p. 1165–76.
[24] Widmann JF. Phase Doppler interferometry measurements in water sprays produced by residential fire sprinklers. Fire Safety J 2001;36(6):545–67.
[25] Dembele S, Wen JX, Sacadura J-F. Experimental study of water sprays for the attenuation of fire thermal radiation. J Heat Transfer 2001;123:534–43.